LANGMUIR

Interface Components: Nanoparticles, Colloids, Emulsions, Surfactants, Proteins, Polymers

Insight into the Molecular Mechanisms of AuNP-based Aptasensor for Colorimetric Detection: a Molecular Dynamics Approach

Witthawat Phanchai, Unnop Srikulwong, Apiwat Chompoosor, Chadamas Sakonsinsiri, and Theerapong Puangmali

Langmuir, **Just Accepted Manuscript** • DOI: 10.1021/acs.langmuir.8b00701 • Publication Date (Web): 03 May 2018

Insight into the Molecular Mechanisms of AuNP-based Aptasensor for Colorimetric Detection: a Molecular Dynamics Approach

Witthawat Phanchai,[†] Unnop Srikulwong,[‡] Apiwat Chompoosor,[¶] Chadamas Sakonsinsiri,[§] and Theerapong Puangmali[*,†,‡]

Materials Science and Nanotechnology Program, Department of Physics, Faculty of Science, Khon Kaen University, Khon Kaen 40002, Thailand, Department of Physics, Faculty of Science, Khon Kaen University, Khon Kaen 40002, Thailand, Department of Chemistry, Faculty of Science, Ramkhamhaeng University, Bangkok 10240, Thailand, and Department of Biochemistry, Faculty of Medicine, Khon Kaen University, Khon Kaen 40002, Thailand

E-mail: theerapong@kku.ac.th

Abstract

Colorimetric aptasensor based on assembly of salt-induced gold nanoparticles (AuNPs) is a promising biosensor. However, the molecular mechanism of the aptasensor is far from being fully understood. Herein, molecular dynamics (MD) simulation was used to investigate molecular interactions in the detection of ochratoxin A (OTA) including: (i) the molecular recognition of the anti-OTA aptamer, (ii) OTA-aptamer interactions in monovalent (Na^+) and divalent (Mg^{2+}) electrolytes, (iii) the binding mode of citrate on the AuNP surface, (iv) interactions of the aptamer with citrate-capped AuNPs and (v) a detailed mechanism of the aptasensor. Our MD simulations revealed a specific binding of the OTA-aptamer complex, compared with OTB and warfarin. Compared with Na^+, Mg^{2+} ions exerted a more effective attractive force between OTA and anti-OTA aptamer. Three different binding modes of citrate on AuNP surfaces were found. The kinetics of the adsorption of unfolded aptamers onto the citrate-capped AuNP was also elucidated. Most importantly, our MD simulation revealed an insightful analysis of the molecular mechanisms in the AuNP-based aptasensor and paved the way for the design of a novel colorimetric aptasensor for other target molecules, which is not limited to OTA detection.

INTRODUCTION

Ochratoxin A (OTA), a type of mycotoxins, is produced by microorganisms such as *Aspergillus* and *Penicillium*. OTA is chemically stable and has a relatively long half-life (35.5 days in humans). Its producers grow easily in various grains like coffee, peanuts, and rice. Additionally, the commercialized food systems like wine, bread, and even meat products can also be contaminated.[1–3] Several studies have introduced OTA as a nephro-, hepato-, neuro-, immunotoxic, and also teratogenic agent.[2] Therefore, it attracts research attention as a new threat to public health and is required to be

*To whom correspondence should be addressed

[†]Materials Science and Nanotechnology Program, Department of Physics, Faculty of Science, Khon Kaen University, Khon Kaen 40002, Thailand

[‡]Department of Physics, Faculty of Science, Khon Kaen University, Khon Kaen 40002, Thailand

[¶]Department of Chemistry, Faculty of Science, Ramkhamhaeng University, Bangkok 10240, Thailand

[§]Department of Biochemistry, Faculty of Medicine, Khon Kaen University, Khon Kaen 40002, Thailand

regulated. To avoid the risk of OTA consumption, it is vitally important to have an appropriate analytical technique for an ultrasensitive detection of OTA.

Aptamer-based biosensor is a promising candidate for a highly sensitive detection of OTA. Aptamers are single-stranded oligonucleotides that are designed through an artificial process named systematic evolution of ligands by exponential enrichment (SELEX).[4] Aptamers exhibit high selectivity and affinity. In addition, they provide a broad range of targets and are easily produced, readily available and highly reproducible and stable.[5] These advantages promote the extensive use of aptamers as the recognition elements in biosensors. Applying aptamers as the recognition elements provides sensitive aptamer-based sensors (aptasensors)[6] which can be used to detect various analytes including antibiotics,[7] toxins,[8] metal ions,[9] and viruses.[10]

In recent years, numerous aptasensors have been introduced for the detection of OTA[11,12] which function through various detection modes.[13–15] Compared with these techniques, colorimetric methods have a simpler sensing mode which allows detection to be made by naked eye.[16] Aptamer-based colorimetric analysis is a method of detection of a target molecule in a solution with the aid of aptamers. There are diverse sensing strategies, and among them colorimetric aptasensor based on analyte-induced aggregation[17]/disaggregation[18,19] of gold nanoparticles (AuNPs) has been frequently reported in the literature. The review of the strategies, mechanisms and recent developments for the use of AuNPs as colorimetric biosensors was recently reported.[20] This sensing strategy is based on the interparticle distance dependence of optical properties of AuNPs. The apparent color of dispersed AuNPs in the solution changes from red to blue after aggregation due to the shift of surface plasmon resonance to a higher wavelength. Therefore, the presence of a particular analyte can be monitored by observing the color change of the solution.

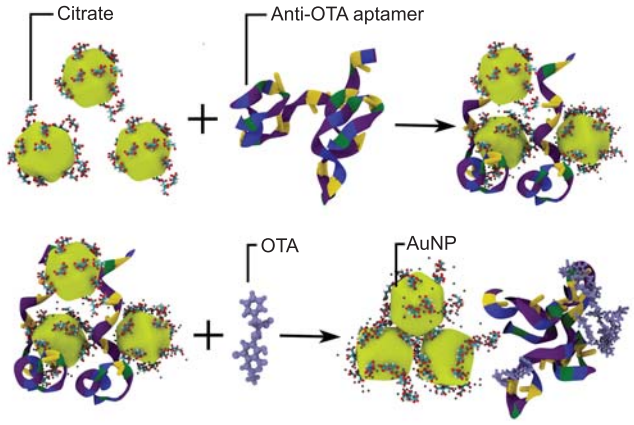

Figure 1: Schematic illustration of the sensing mechanism of AuNP-based colorimetric aptasensor for OTA detection. The colors of anti-OTA aptamer represent different nitrogenous bases. Adenine (A), thymine (T), cytosine (C) and guanine (G) correspond to blue, yellow, green and purple, respectively.

AuNPs-based aptasensor can be typically divided into two categories: (i) unfunctionalized AuNPs aptasensors and (ii) DNA-functionalized AuNPs aptasensors. In unfunctionalized AuNPs aptasensors, the unfolded aptamers can adsorb onto the negatively-charged AuNPs, thus preventing AuNPs from aggregating in saline solution as illustrated in Figure 1. When aptamers turn into a target-aptamer complex, they will be released from the AuNPs, so the addition of NaCl leads to the aggregation of the AuNPs.[21] For the DNA-functionalized AuNPs aptasensors, disassembly of preformed DNA-functionalized AuNP dimers by analyte induction is another successful method which proves superior to unmodified AuNPs aptasensors in terms of stability, sensitivity and detection range.[18] To obtain higher analytical figures of merit, deeper understanding on the sensing mechanisms of the aforementioned strategies is required. However, there have been only a limited number of theoretical works[22] examining features of interactions of an anti-OTA aptamer with OTA. In addition, deeper molecular-level analysis of the sensing mechanisms for OTA detection has not been revealed yet, despite a large volume of experimental reports[17–19] of the aptamer-based biosensor.

In light of this, we performed a computa-

tional modeling, based upon molecular dynamics (MD) simulation, to gain an insight into the molecular mechanisms of a colorimetric aptasensor. MD simulation was used to (i) investigate recognition interactions between the anti-OTA aptamers and OTA molecules. Our study shows recognition sites of the anti-OTA aptamer and provides a deeper understanding of the binding interaction. The specificity of the anti-OTA aptamer can be performed by MD simulation. Besides, (ii) the influences of monovalent (Na^+) and divalent (Mg^{2+}) electrolytes on the binding interaction and stabilities of the OTA-aptamer complexes have been observed. Furthermore, (iii) a detailed picture of the AuNPs and binding modes of citrate was obtained by computational modeling. Elucidating the binding mode of carboxylate-containing ligands to AuNPs is crucial to the understanding of their stabilizing role as a sensor probe. This is of great importance for the insightful discussion of the assembly and disassembly of AuNPs. (iv) The binding of anti-OTA aptamer onto the AuNP surface was taken into account. Finally, (v) the sensing mechanisms for OTA detection, but not limited to, can be clearly understood by our *in silico* study which can also be used to explain the experiment of Yang and co-workers[21] and related works.[18]

METHOD

Force Fields of AuNPs and Biomolecules

The nanocrystalline structure of the AuNP is characterized as a face-centered cubic (FCC) lattice structure. The equilibrium shape of the AuNP is a modified truncated octahedron.[23] A 2-nm-in-diameter AuNP, composed of 309 Au atoms, was constructed by cutting the crystal out of a bulk gold face-centered cubic lattice. The oxidation state of Au atoms is Au(0).[24] The transferable AMBER-compatible force field parameters for AuNP was obtained from the literature.[25] For the single-stranded DNA (ssDNA) aptamer, the structure of the DNA was generated by NAFlex,[26] an on-line web server that offers a variety of simulation methods to obtain a dynamic view of nucleic acid structures. The sequence of anti-OTA aptamer is 5′-GAT CGG GTG TGG GTG GCG TAA AGG GAG CAT CGG ACA-3′.[18,21] Each nucleobase is hereafter denoted as BX, where B and X are a nucleobase and the order of the nucleobase from the 5′ end, respectively. It was experimentally found that the anti-OTA aptamer has high binding affinity with OTA molecules and possesses the ability to induce the formation of antiparallel G-quadruplex structure.[21] The force field for DNA atomistic simulation is AMBER parmBSC1[27] which had been parametrized from high-level quantum mechanical data.[28] AMBER parmBSC1 was tested by Ivani and co-workers[27] for nearly 100 systems and evaluated for a total simulation time of 140 μs which covered most of the DNA structures. For the biomolecules used in the simulation, including ochratoxin A, ochratoxin B (OTB), warfarin and citrate, the Hartree-Fock theory from Gaussian09 software package using HF/631G* method was used to optimize the structures, whereas the partial charges were derived from using ANTECHAMBER.[29] All force field parameters can be found in the supplementary information (SI) in Table S1 and Table S2.

Hybrid Solvation

Since the ssDNA aptamer contains 36 bp, the simulation box is relatively large and the calculation consumes expensive computational resources. The accurate simulation of such a biomolecular system depends upon the solvation effect. As the solute-solvent distance increases, the properties of water tend to become similar to those of the bulk liquid. The bulk area could therefore be represented by a coarse-grained (CG) solvent model whereas the water around the solute was considered in atomistic details.[30,31] In our hybrid model, the system consists of a ssDNA aptamer, target molecules and citrate-capped AuNPs, surrounded by a shell of atomistic waters (TIP3P), embedded in CG molecules, called WatFour (WT4), to represent bulk water. In the WT4 water model,

eleven water molecules are grouped into four tetrahedrally interconnected beads.[32] This can effectively mimic the dynamics of molecular systems composed of pure all-atom water. After the insertion of the ssDNA aptamer, counterions (Na^+ and Cl^-) were added to the solvents (both atomistic and CG shells) to ensure electroneutrality. Compared with all-atom model having the same simulation box size ($16.5\times16.5\times16.5$ nm^3), the number of water molecules was dramatically reduced from 444824 atoms to 90463 atoms. This hybrid solvation provides a significant reduction of the number of water molecules leading to significantly faster simulation time. In addition to a reduction in the computational cost, it opens the door for its employment to study the biological processes which occur on space and time scales that are often unreachable for fully atomistic simulation.

Simulation Details

All simulations were performed by the GROMACS 5.0.4 package[33] with a time step of 2 fs. The LINCS algorithm was applied to all bonds connected to hydrogen atoms. The Lennard-Jones potential was applied to estimate van der Waals interaction with a cut-off radius of 1.2 nm for gold atoms, and $\sigma = 2.629e^{-1}$ nm and $\varepsilon = 22.133$ kJ/mol. The system temperature was set at 300 K. Berendsen temperature coupling and Parrinello-Rahman pressure coupling were used to set the system in an NPT ensemble. Time constant for pressure coupling (1 bar) was 6 ps. The particle mesh ewald (PME) method was applied to calculate the long-range electrostatic interactions. All visualizations were done with Visual Molecular Dynamics (VMD).[34]

RESULTS AND DISCUSSION

Molecular Recognition of Anti-OTA Aptamer

Anti-OTA aptamers are functional ssDNA obtained from a random oligonucleotide library through SELEX technique.[35] Although the anti-OTA aptamer,[18,21] which binds to OTA with high affinity and specificity, has been widely used and developed into a novel detection method for the toxin, the binding interaction between the unfolded anti-OTA aptamer and OTA is still not clear. To confirm the affinity and specificity between the aptamer and the target molecule, we carried out MD simulations to compare the molecular recognition among three different structures including OTA, OTB and warfarin. The chemical structures and the molecular recognition of these target molecules are illustrated in Figure 2.

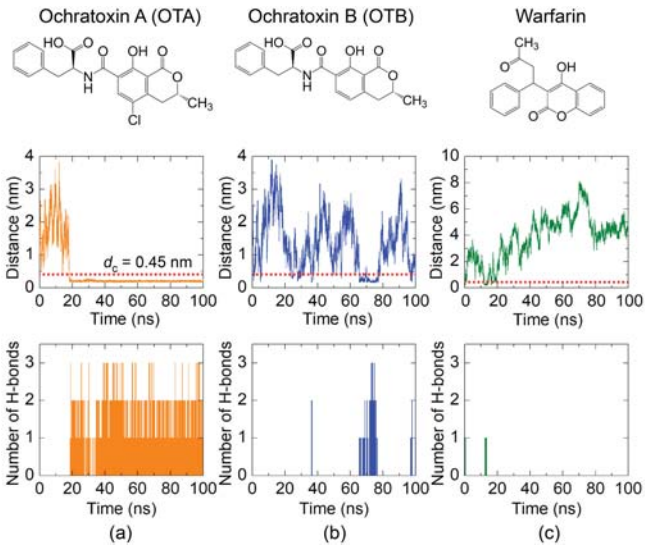

Figure 2: Recognition interaction of anti-OTA aptamer. The minimum distance between target molecules and the aptamer and the number of hydrogen bonds between target molecules and the aptamer with the simulation time of 100 ns. The target molecules include (a) ochratoxin A, (b) ochratoxin B and (c) warfarin. The dashed line shows a cut-off distance of 0.45 nm to define non-covalent binding.

OTA and structural analogues of OTA, i.e., OTB and warfarin, were used to evaluate the selectivity and specificity of the aptamer. The molecular interaction between the aptamer and these target molecules was observed by MD simulations for 100 ns. Basically, the binding interaction between the aptamer and the target molecule is a result of non-covalent bonding consisting of van der Waals forces, hydrogen bonds and electrostatic interactions.[36,37] van der Waals interactions typically extend to a distance of 0.6 nm for large biomolecules. In the present simulation systems, we conservatively used a cut-off distance (d_c) of 0.45 nm as the distance to define non-covalent OTA-aptamer binding. Accordingly, the OTA-aptamer combination is considered to be in a bound configuration provided that the distance between atoms within the binding region is lower than d_c for a minimum of 20 ns. For the hydrogen bonding, the hydrogen bond is considered to have a maximum distance of 0.35 nm and a corresponding angle of 30° or less between the donor and acceptor atoms.[37]

To perform the binding simulations, OTA, OTB and warfarin were placed in the same simulation box. For the OTA, it was found that there were two states of the binding complex. As shown in Figure S1, at t = 16 ns, OTA could bind with C17, G18, T19 and A20 of the aptamer and the binding continued until t = 36 ns. Subsequently, the OTA strongly bound with three nubleobases including G16, C17 and A21 and remained bound with these bases until the end of the simulation. A bound configuration was observed at t = 20 ns (see Figure 2(a)). At this state, the distance between the OTA molecule and the binding sites fell below d_c and remained below the cut-off distance for the remainder of the simulation. It was noticeable that the OTA frequently bound with three nucleobases including G16, C17 and A21. The interactions between the 21st adenine nucleotide (A21) were present throughout the OTA-aptamer complex simulations. This suggests that A21 plays an important role in the molecular binding.

Hydrogen bond analysis could be used to identify such a structural change, since the aptamer tertiary structure was held together by hydrogen bonding. As can be seen in Figure 2, the formation of hydrogen bonds generally corresponded with the minimal contact distance. In other words, when OTA was close to one of the aptamer bases, hydrogen bonds formed simultaneously. This was in accordance with the number of hydrogen bonds of the OTA-aptamer complex, as illustrated in Figure 2(a). A detailed analysis of hydrogen bond formation between atoms within an OTA-aptamer binding complex reveals that there are two states of complex formation. The atom indexes in OTA are shown in Figure S2. In the initial state, hydrogen bonds are formed between hydrogen atoms of OTA and oxygen atoms of C17, G18 and T19 of the aptamer. The indexes of each oxygen atom in C17, G18 and T19 are shown in Figure S3(a)-(c). The hydrogen bonds at the initial state are due to the interactions between H9-O2(C17), H16-O2P(G18) and H8-O4(T19). As can be seen, the number of hydrogen bonds formed at the initial state is less than those found in the bound state (Figure S4). In other words, in the initial state solely weak interactions are observed. The second state involving of stronger bonding of atoms is stronger than in the initial one. The favored interactions are due mainly to the hydrogen bonding between oxygen atoms of OTA and hydrogen atoms of A21. Key atoms that form the hydrogen bonds between OTA and the aptamer are O1-H62(A21), O2-H62(A21) and O3-H62(A21), as illustrated in Figure S4. During the bound state, the number of hydrogen bonds fluctuated with a maximum number of hydrogen bonds of three. During this time, the aptamer structure reorganized to a stable conformation. Towards the end of the simulations, the variation within the number of hydrogen bonds in the aptamer structure was found to be minimal. Apart from C17, G18, T19 and A21, other nucleobases could also serve as binding positions from time to time. To sum up, the binding sites of the anti-OTA aptamer at the stable state included the following nucleotide bases: G1, G16, C17, G18, T19, A20, A21, G27, C28, G33, and A34.

To ensure the specificity of the anti-OTA aptamer, we then observed the molecular recogni-

tions between the anti-OTA aptamer and OTB and warfarin. Hydrogen bond analysis and the distance between the aptamer and the target molecules could identify the molecular selectivity of the aptamer. Those molecules could not bind with the aptamer and the significant formation of hydrogen bonding was not found, as illustrated in Figure 2(b)-(c). Our simulation confirms the recognition interactions of the anti-OTA aptamer and is in good agreement with the experiment in which the aptamer bound with a 100-fold less affinity to OTB and did not form compounds with warfarin.[35]

Besides, we also performed the simulations to verify the molecular recognition of the widely-used sequence by shortening the aptamer. The binding between OTA and three different modified aptamer sequences was conducted. The distance between OTA and aptamer, and the number of H-bonds of three modified sequences are illustrated in Figure S5. For the sequence (a), the anti-OTA aptamer was shortened by removing twelve nucleobases from the 3′ end. In the case of the sequence (b), six nucleobases were removed from both 3′ and 5′ ends. The sequence (c) was modified by substituting G11 by a cytosine residue and three additional nucleobases (ACG) were added at the 3′ end, highlighted in red. It was found that the modification of the anti-OTA aptamer sequences induces losses of affinity and specificity, as shown in Figure S5(a)-(c). Compared with OTA, the binding with OTB is stronger for the sequence (a) (Figure S5(a)). In other words, the specificity is lost once the sequence of anti-OTA aptamer is modified. To sum up, the binding ability is sequence dependent. This is in accordance with the experimental findings.[35]

Since the binding interactions depend upon the environment of the system such as solvents, in the following section, the effect of monovalent and divalent electrolytes on the binding of OTA and aptamer will be taken into consideration.

OTA-aptamer Interactions in Monovalent and Divalent Electrolytes

The structures and functions of nucleic acids are sensitively correlated with the "counterion atmosphere" owing to their polyelectrolyte nature.[38] DNA is negatively charged due to its sugar-phosphate backbone and the partial negative charge in the OTA molecule is a result of carboxyl, carbonyl, ester, and chloro groups. Consequently, the interaction between the ssDNA aptamer and OTA is primarily through electrostatic and van der Waals forces. The counterions around the ssDNA aptamer and OTA plays a key role in electrostatic screening which reduces the repulsion between these biomolecules. Divalent ions (Mg^{2+}), compared with monovalent ions (Na^{+}), have stronger interactions with nucleic acids.[38] Li and co-

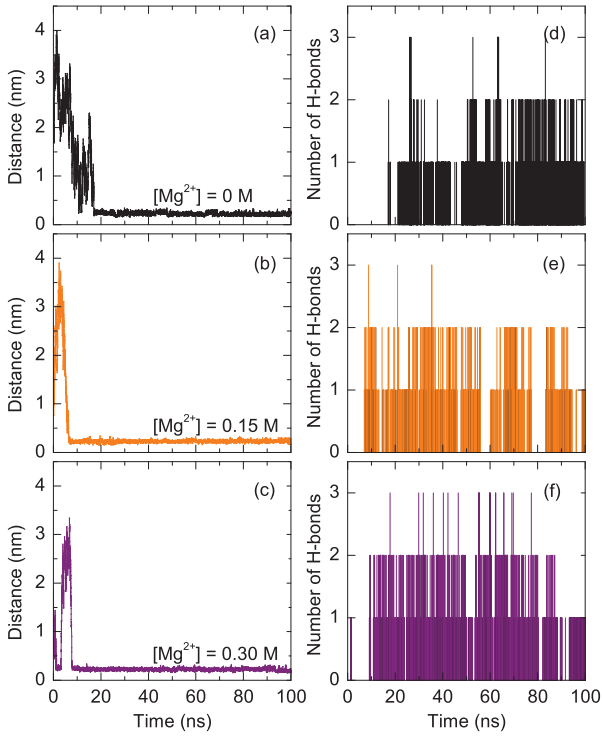

Figure 3: (a)-(c) The minimum distance between the aptamer and OTA versus time with different magnesium ion concentrations [Mg^{2+}]. (d)-(f) The number of hydrogen bonds between OTA and the aptamer with the [Mg^{2+}] = 0, 0.15 and 0.30 M, respectively. The salt concentration of all simulations is 0.15 M.

workers reported[38] that Mg^{2+} ions have stable hydration shells and stronger interaction with DNA. Cruz-Aguado and Penner[35] selected various aptamers that can bind OTA with various affinities. In this work, the effect of the magnesium concentrations on the aptamer-OTA binding affinity was analyzed, and the binding was found to depend on the presence of Mg^{2+}. Since the counterions are highly dynamic, it is difficult for experimentalists to provide a microscopic description. In addition, the detailed atomistic interacting picture of the effect of divalent electrolytes on the OTA-aptamer interaction is scarcely documented.

In the present study, the effects of Mg^{2+} ions, in comparison with those of Na^+, on OTA-aptamer binding interaction were studied by MD simulations. It was found that Mg^{2+} ions prefer to bind to the oxygen atom in the phosphate backbone through electrostatic interaction. When the anti-OTA aptamer was in close proximity to the OTA molecule, Mg^{2+} ions accumulated at the interfacial area and formed ion-dipole interaction and electrostatic interaction with chloro group in the OTA molecule and oxygen in the phosphate group, respectively, like "bridging" them together (see Figure S6). These Mg^{2+} ions exerted an effective attractive force between the two molecules. Both OTA and anti-OTA aptamer can "clamp" onto the Mg^{2+} ion. The O to Mg^{2+} distance is 3.91 Å, whereas the distance between Cl atom of the OTA molecule and Mg^{2+} is 5.67 Å. It plays more important role than Na^+ ions as the monovalent cations bind to DNA in a quite diffusive manner which is much weaker than that of a divalent bridge.[38] Therefore, the binding between OTA and the aptamer in the Mg^{2+} electrolyte is faster than in monovalent electrolyte as one can see from the distance (Figure 3(a)-(c)) and hydrogen bonding (Figure 3(d)-(f)) between OTA and anti-OTA aptamer. However, an increase in Mg^{2+} concentration, as shown in Figure 3, has no significant effect on the binding time of OTA-aptamer complex. Our computational results are consistent with the experimental data published by Cruz-Aguado and Penner.[35]

Binding Mode of Citrate in the Stabilization of AuNPs

The binding of citrate ligands to AuNPs is crucial for the stabilization of AuNPs.[39] It is accepted that the region surrounding the citrate-capped AuNP is negatively charged due to anionic carboxylate groups. A more detailed picture of the interactions between the gold surface and the citrate ligand was recently reported by Al-Johani and co-workers.[24] By combining solid-state NMR, TEM, XPS and DFT calculations, they proposed reasonable structures and modes of interaction for citrate-stabilized AuNP surfaces. Based on DFT calculations, they concluded that there were various binding geometries between carboxylate-containing ligands and Au model surfaces and presented evidence for three different modes: monocarboxylate monodentate ($1\kappa O^1$), monocarboxylate bridging ($\mu_2 - 1\kappa O^1 : 2\kappa O^3$), and dicarboxylate bridging ($\mu_4 - 1\kappa O^1 : 2\kappa O^3 : 3\kappa O^{1'} : 4\kappa O^{3'}$). XPS experiments indicated that AuNP surface atoms were mainly in the zero oxidation state Au(0). ^{23}Na NMR and TEM/EDS experiments also suggested that Na^+ ions were present near the gold surface.

In the present work, the mechanism of citrate anions adsorbed onto the AuNP surface in an electrolyte solution was characterized in detail. Our computational results confirmed recent experimental findings[24] regarding the characteristic binding modes of citrate anions on the AuNP surface. The simulation was performed at a temperature of 373 K with the citrate:Au molar ratio being 0.2:1. All surface gold atoms were in the zero oxidation state as reported in the literature.[24,40] After the system was equilibrated for 35 ns, the number of adsorbed citrate anions on a 2-nm-in-diameter AuNP surface was 19 anions, corresponding to the surface density of 1.58 anions/nm^2. We found that the Au(111) surface was the most populated facet to which the citrate anions bound due to its lowest surface energy.[14] The formation of citrate on Au(110) and Au(100) surfaces is less favorable We then investigated the binding mode of the carboxylate-containing ligands to AuNP. The binding mode was examined by the dis-

tance between the citrate anion and gold atoms on the surface. Guided by the MD simulations, we found various binding geometries between the carboxylate group and the AuNP surface and three different modes were present as shown in Figure 4. The geometry with only one carboxylate oxygen interacting with one Au is referred to monocarboxylate monodentate (κ), as shown in Figure 4(a). The distance between O1 and Au atom was 0.33 nm. However, the transformation of the binding could be observed at $t = 82$ ns. As a result, O2 could bind with Au atom instead of O1. Our Au-O distance was close to that obtained from a DFT calculation falling in the range of $0.22 - 0.24$ nm.[24] Our simulations also suggested that Na^+ ions were present near the gold surface due to the binding between Na^+ ions and oxygen atoms in the carboxylate group (Figure 4). As illustrated in Figure S7, more Na^+, compared with Cl^-, were present around the AuNP surface. This is in accordance with the ^{23}Na NMR experiments.[24] In addition to the κ coordination mode, monocarboxylate bridging (μ_2) and dicarboxylate bridging (μ_4) were also found, as one can see in Figure 4(b)-(c). In the μ_2 fashion, two Au-O binding motifs were formed at the gold surface. The resonance of electrons was responsible for this binding mode where three Na^+ ions were also found at the surface. Additionally, the μ_4 motif could also be observed in which two terminal carboxylates were involved in the binding interactions. It is worth noting that most citrates have μ_2 motif (eight and two citrates on Au(111) and Au(100), respectively). Four citrates with the μ_4 fashion have been observed on Au(100) and two molecules have κ coordination mode on Au(111). Three citrate anions are in the secondary shell.

Understanding the binding mode of the citrate ligands on the AuNP surface leads to a complete understanding of the fundamental adsorption of ssDNA onto citrate-capped AuNP surfaces which will be discussed in the following section.

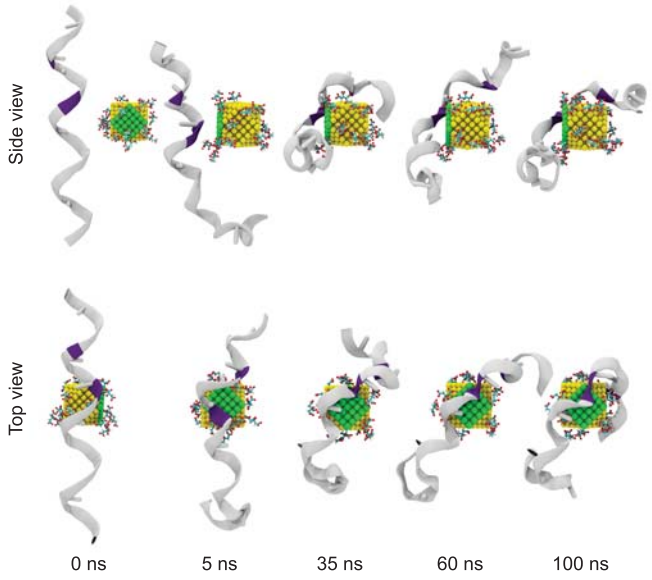

Figure 5: ssDNA adsorption through displacement of citrate on AuNP surface. The green color represents the Au(100) plane. The number of citrate anions on the adsorbed plane is decreased with increasing time due to the electrostatic repulsion between the negatively charged phosphate backbone and citrate anions. Solvents and ions were not shown for clarity. The simulation was performed for 100 ns.

Interactions of Anti-OTA Aptamer with Citrate-capped AuNPs

ssDNA can be adsorbed by citrate-capped AuNPs, resulting in an increased AuNP stability, which forms the basis of a number of biochemical and analytical applications. The mechanism of nonthiolated ssDNA adsorption, however, remains unclear. AuNPs are capped with negatively charged citrate, posing an electrostatic barrier for adsorbing negatively charged ssDNA. ssDNA adsorption must, therefore, be achieved by non-ionic forces. It has been observed that different bases show different binding affinities,[41,42] highlighting the importance of specific nucleobase-Au interaction. While there is extensive literature about the adsorption of bases, nucleosides and nucleotides in thin films of different metals such as gold,[43] silver[44] and even copper,[45] in the case of NPs, particularly AuNPs, studies are rather scarce.

As the mechanism is still unclear, different models have been suggested. Recently, a mechanism has been proposed whose key lies in the stabilizing force caused by the interaction between the nucleotides and the AuNP.[46] According to this model, the ssDNA needs to approach the particle in order to displace the citrate and is then adsorbed in a latter step. The neutralization of the negative charges by salt addition favors the process and provides screening long range electrostatic repulsions. Upon adsorption, the DNA may change conformation to maximize contact points with the surface. The adsorbed molecules of DNA create a zone where other biopolymer molecules cannot get near and subsequent saturation of the surface with those zones impedes adsorption of further DNA molecules.

In this work, the binding interaction between DNA aptamer and a 2-nm-in-diameter AuNP has been investigated. The simulation was performed for 100 ns. Based upon our simulations, we suggest the following mechanism to describe the ssDNA adsorption. Since the backbone of the oligonucleotide is negatively charged, the electrostatic repulsion between the ssDNA and citrate anions results in the repulsion of citrate anions to neighbouring surfaces, as illustrated in Figure 5. The electrostatic interaction not exclusively determines adsorption kinetics but also influences the binding capacity. At $t = 0$ ns, three citrate anions were on Au(100) plane. Once adsorbed, the ssDNA aptamer changes its conformation on the surface to maximize the surface contact. Due to the electrostatic repulsion, citrate anions on the AuNP surface were then repelled to the neighboring crystal planes and at $t = 5$ ns, there was no citrate anion on the Au(100) plane (green color), resulting in the formation of an area electrostatically excluded to the ssDNA aptamer. The adsorption of oligonucleotide on the AuNP surface can be further examined by the distance between the nucleotide and the gold surface. As presented in Figure 6(a)-(b), the phosphates of G9, G15 and G16 are in close proximity to the AuNP surface thus repulsing citrate anions to the neighbouring planes. At $t = 0$ ns, the distances between the phosphates of G9, G15, G16 and

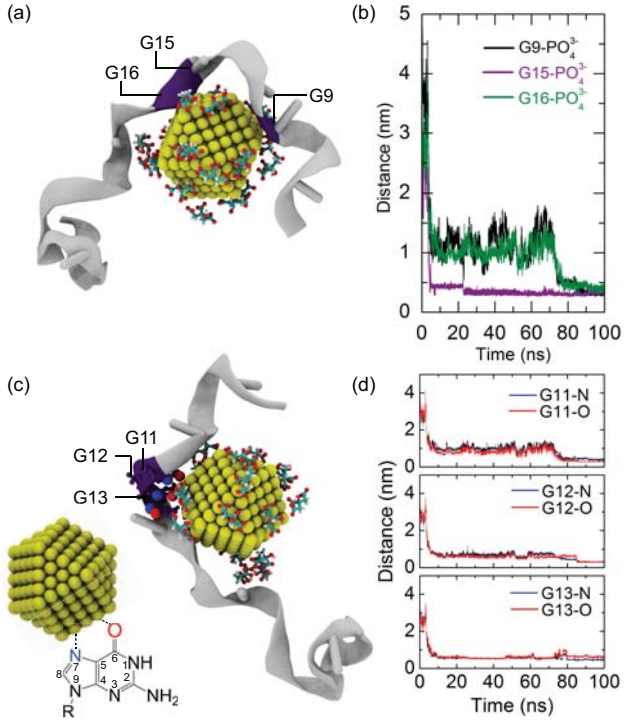

Figure 6: Adsorption of oligonucleotide on the AuNP surface. (a) Snapshot of backbone binding interaction at $t = 100$ ns, (b) distance between phosphate and AuNP versus time, (c) snapshot of nucleoside binding interaction at $t = 100$ ns and the proposed structure for the AuNP interaction with guanine[47] (The dashed lines represent non-bonded interactions.), and (d) the distance between N and O of the nitrogenous bases and AuNP versus time.

the Au(100) plane were more than 4 nm. Due to the presence of the oxygen in the carbonyl group and N(7) nitrogen atom, guanines have a strong tendency to bind to AuNP through non-bonded interaction.[48] G9 was attached on Au(111), whereas G15 and G16 were in close proximity to Au(100). The adsorption involves the oxygen of the C(6) carbonyl group and the N(7) atoms of G11, G12 and G13, as shown in Figure 6(c)-(d). The physisorption process of ssDNA on the AuNP surface is through guanine moiety which is in good agreement with the binding interaction proposed by Pergolese and co-workers.[47]

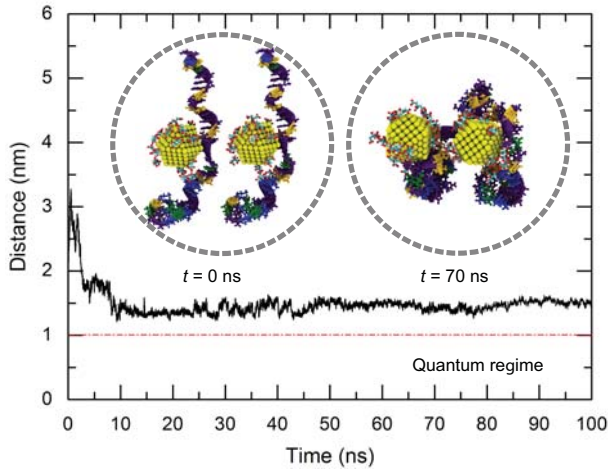

Figure 7: Interparticle distance between two aptamer-bound AuNPs as a function of time. The salt concentration is 0.15 M. The insets show the interactions between AuNPs at $t = 0$ and $t = 70$ ns. The interparticle distance remained higher than the threshold distance (1 nm) for a 100 ns simulation, due to the electrostatic repulsion from ssDNA which prevents van der Waals attractions and enhances the stability of AuNPs against salt-induced aggregation.

Mechanism of Aptasensor for OTA Detection

The unique optical properties of AuNPs, due to localized surface plasmons excited by incident electromagnetic field of specific energy, have attracted great interest in the past decades because of several associated applications such as ultrasensitive biological and chemical sensing. The localized surface plasmon resonance (LSPR) can be understood as a collective resonant oscillation of free electrons within a metal nanoparticle in response to an incident electromagnetic radiation. When the NPs are in close proximity, the individual surface plasmons can couple, leading to a shift in the optical response. Surface plasmon coupling depends on the way the NPs are assembled. Theoretical studies by Nordlander and co-workers revealed that quantum tunneling effects begin to disturb the interaction between the surface plasmons when the interparticle distance (d) is below 1 nm.[49–51] As the gap distance continues to decrease below a "threshold tunnel-distance" (d_{th}), the electron tunneling effect completely modifies the behavior of the plasmonic response in the quantum regime.[52] Therefore, variations in the assembly parameters, i.e., interparticle distance, configuration and the number of NPs, allow one to finely tune the resonance wavelength. Since the plasmonic response of AuNPs is interparticle distance dependent, the assembly of citrate-capped AuNPs in the saline solution was observed. We initially investigated the aggregation of two citrate-capped AuNPs in the NaCl solution with the concentration of 0.15 M. The initial interparticle distance was 5 nm and fell below 1 nm within $\sim$ 5 ns, as illustrated in Figure S8. The addition of NaCl would screen the charge on the surface of AuNPs, resulting in an aggregation ($d < d_{\mathrm{th}}$). To prevent the aggregation of AuNPs, citrate-capped AuNPs were modified with ssDNA aptamers. Subsequently, we performed an MD simulation for two aptamer-bound AuNPs in a saline solution ([NaCl]= 0.15 M). The interparticle distance was initially 3 nm and it remained higher than the threshold distance ($d > d_{\mathrm{th}}$) for a 100 ns simulation, as shown in Figure 7. This is due to the electrostatic repulsion from ssDNA and steric hindrance which prevent van der Waals attractions and enhances the stability of AuNPs against salt-induced aggregation.

Disassembly of such AuNPs can be induced by OTA, the target molecules of the anti-OTA aptamer. Upon the addition of OTA, the specific binding interaction between OTA and anti-OTA aptamer resulted in the desorption of the aptamer from the AuNP surface, as shown in Figure 8. This prevented the exposure of the aptamer bases to AuNPs, and thus the ability to protect AuNPs at a high-salt concentration was lost. The initial interparticle distance between AuNPs was 2.5 nm. At $t = 43$ ns, the binding interactions of OTA/anti-OTA aptamer was found and then the interparticle distance of AuNP-AuNP slightly decreased. At $t = 400$ ns, the interparticle distance nearly reached 1 nm. The plot of the interparticle distance as a function of time is shown in Figure S9. It is computationally expensive to perform the simulation until the aptamer is com-

pletely released from the AuNP surface. However, it is expected that after the complete release of the DNA aptamer, the AuNPs will be aggregated at a high salt concentration, as previously discussed in Figure S8. From the experimental point of view, as the optical properties of the AuNPs depends upon the interparticle distance, the color of the solution changes with the decrease in interparticle distance and can be observed by naked-eye. Owing to the interparticle-distance dependent optical properties, this simple colorimetric method can be applied to colorimetric biosensors which are not exclusively limited to OTA detection.

CONCLUSIONS

The hybrid solvation model was used to examine the molecular recognition at atomistic level. The binding interactions of the anti-OTA aptamer and OTA were clearly elucidated. Our simulations revealed the strong binding zones of the anti-OTA aptamer including G1, G16, C17, G18, T19, A20, A21, G27, C28, G33, and A34. The binding was evaluated by the intermolecular distances and the number of hydrogen bonds. The divalent electrolyte (Mg^{2+}) played an essential role as a bridging ion in the binding interactions. The anti-OTA aptamer is capable of binding with OTA specifically, compared with OTB and warfarin. The binding mode of citrate and gold atoms was elucidated. Three different binding modes were found on the AuNP surface including monocarboxylate monodentate (κ), monocarboxylate bridging (μ_2), and dicarboxylate bridging (μ_4). Au(111) was the favorite binding plane of citrate. Salt-induced aggregation of citrate-capped AuNPs was a result of electrostatic screening. The adsorption of the anti-OTA aptamer onto the surface of the citrate-capped AuNPs was due to nucleoside and backbone binding motif. The unfolded aptamers could adsorb onto the negatively-charged AuNPs, thus preventing AuNPs from aggregating in salt solution. Upon the addition of OTA, the specific binding interaction between OTA and anti-OTA aptamer resulted in the desorption of the aptamer from the AuNP surface. This prevented the exposure of the aptamer bases to AuNPs, and thus the ability to protect AuNPs under high-salt conditions was lost. Our MD simulation revealed an insightful discussion of the molecular mechanisms in the AuNP-based aptasensor and paved the way for the design of a novel colorimetric aptasensor.

ASSOCIATED CONTENT

Supporting Information

The Supporting Information is available free of charge on the ACS Publications website at DOI: xx.xxx/acs.langmuir.xxxxxx.

AUTHOR INFORMATION

Corresponding Author

*E-mail: theerapong@kku.ac.th.

ORCID

Theerapong Puangmali: 0000-0003-2529-7528

Notes

The authors declare no competing financial interest.

Acknowledgement We would like to express our appreciation to Bureau of Information Technology, Khon Kaen University, for the computational resource. WP would also like to express our gratitude to Science Achievement Scholarship of Thailand for financial support.

References

(1) Chrouda, A.; Sbartai, A.; Baraket, A.; Renaud, L.; Maaref, A.; Jaffrezic-Renault, N. An Aptasensor for Ochratoxin A based on Grafting of Polyethylene Glycol on a Boron-doped Diamond Microcell. *Anal. Biochem.* **2015**, *488*, 36 – 44.

(2) El Khoury, A.; Atoui, A. Ochratoxin A: General Overview and Actual Molecular Status. *Toxins* **2010**, *2*, 461–493.

(3) Wang, C.; Dong, X.; Liu, Q.; Wang, K. Label-free Colorimetric Aptasensor for Sensitive Detection of Ochratoxin A Utilizing Hybridization Chain Reaction. *Anal. Chim. Acta* **2015**, *860*, 83 – 88.

(4) Blank, M.; Blind, M. Aptamers as Tools for Target Validation. *Curr. Opin. Chem. Biol.* **2005**, *9*, 336 – 342.

(5) Zhang, J.; Zhang, X.; Yang, G.; Chen, J.; Wang, S. A Signal-on Fluorescent Aaptasensor based on Tb^{3+} and Structure-switching Aptamer for Label-free Detection of Ochratoxin A in Wheat. *Biosens. Bioelectron.* **2013**, *41*, 704 – 709.

(6) Chauhan, R.; Singh, J.; Sachdev, T.; Basu, T.; Malhotra, B. Recent Advances in Mycotoxins Detection. *Biosens. Bioelectron.* **2016**, *81*, 532 – 545.

(7) Seo, H. B.; Kwon, Y. S.; Lee, J.-e.; Cullen, D.; Noh, H. M.; Gu, M. B. A Novel Reflectance-based Aptasensor using Gold Nanoparticles for the Detection of Oxytetracycline. *Analyst* **2015**, *140*, 6671–6675.

(8) Tang, J.; Xie, J.; Shao, N.; Yan, Y. The DNA Aptamers that Specifically Recognize Ricin Toxin Are Selected by Two In Vitro Selection Methods. *Electrophoresis* **2006**, *27*, 1303–1311.

(9) Song, S.; Wang, L.; Li, J.; Fan, C.; Zhao, J. Aptamer-based Biosensors. *TrAC, Trends Anal. Chem.* **2008**, *27*, 108 – 117.

(10) Torres-Chavolla, E.; Alocilja, E. C. Aptasensors for Detection of Microbial and Viral Pathogens. *Biosens. Bioelectron.* **2009**, *24*, 3175 – 3182.

(11) Hayat, A.; Sassolas, A.; Marty, J.-L.; Radi, A.-E. Highly Sensitive Ochratoxin A Impedimetric Aptasensor based on the Immobilization of Azido-aptamer onto Electrografted Binary Film via Click Chemistry. *Talanta* **2013**, *103*, 14 – 19.

(12) Tong, P.; Zhang, L.; Xu, J.-J.; Chen, H.-Y. Simply Amplified Electrochemical Aptasensor of Ochratoxin A based on Exonuclease-catalyzed Target Recycling. *Biosens. Bioelectron.* **2011**, *29*, 97 – 101.

(13) Yuan, Y.; Wei, S.; Liu, G.; Xie, S.; Chai, Y.; Yuan, R. Ultrasensitive Electrochemiluminescent Aptasensor for Ochratoxin A Detection with the Loop-mediated Isothermal Amplification. *Anal. Chim. Acta* **2014**, *811*, 70 – 75.

(14) Park, J.-H.; Byun, J.-Y.; Mun, H.; Shim, W.-B.; Shin, Y.-B.; Li, T.; Kim, M.-G. A Regeneratable, Label-free, Localized Surface Plasmon Resonance (LSPR) Aptasensor for the Detection of Ochratoxin A. *Biosens. Bioelectron.* **2014**, *59*, 321 – 327.

(15) Chen, J.; Zhang, X.; Cai, S.; Wu, D.; Chen, M.; Wang, S.; Zhang, J. A Fluorescent Aptasensor based on DNA-scaffolded Silver-nanocluster for Ochratoxin A Detection. *Biosens. Bioelectron.* **2014**, *57*, 226 – 231.

(16) Feng, C.; Dai, S.; Wang, L. Optical Aptasensors for Quantitative Detection of Small Biomolecules: A Review. *Biosens. Bioelectron.* **2014**, *59*, 64 – 74.

(17) Guo, L.; Xu, Y.; Ferhan, A. R.; Chen, G.; Kim, D.-H. Oriented Gold Nanoparticle Aggregation for Colorimetric Sensors with Surprisingly High Analytical Figures of Merit. *J. Am. Chem. Soc.* **2013**, *135*, 12338–12345.

(18) Xiao, R.; Wang, D.; Lin, Z.; Qiu, B.; Liu, M.; Guo, L.; Chen, G. Disassembly of Gold Nanoparticle Dimers for Colorimetric Detection of Ochratoxin A. *Anal. Methods* **2015**, *7*, 842–845.

(19) Wang, F.; Liu, S.; Lin, M.; Chen, X.; Lin, S.; Du, X.; Li, H.; Ye, H.; Qiu, B.;

Lin, Z.; Guo, L.; Chen, G. Colorimetric Detection of Microcystin-LR based on Disassembly of Orient-aggregated Gold Nanoparticle Dimers. *Biosens. Bioelectron.* **2015**, *68*, 475 – 480.

(20) Aldewachi, H.; Chalati, T.; Woodroofe, M. N.; Bricklebank, N.; Sharrack, B.; Gardiner, P. Gold Nanoparticle-based Colorimetric Biosensors. *Nanoscale* **2018**, *10*, 18–33.

(21) Yang, C.; Wang, Y.; Marty, J.-L.; Yang, X. Aptamer-based Colorimetric Biosensing of Ochratoxin A Using Unmodified Gold Nanoparticles Indicator. *Biosens. Bioelectron.* **2011**, *26*, 2724 – 2727.

(22) Motycka, J.; Mach, P.; Melichercik, M.; Urban, J. DFT and MD Study of the Divalent-cation-mediated Interaction of Ochratoxin A with DNA Nucleosides. *J. Mol. Model.* **2014**, *20*, 2274.

(23) Barnard, A. S.; Lin, X. M.; Curtiss, L. A. Equilibrium Morphology of Face-Centered Cubic Gold Nanoparticles >3 nm and the Shape Changes Induced by Temperature. *J. Phys. Chem. B* **2005**, *109*, 24465–24472.

(24) Al-Johani, H. et al. The Structure and Binding Mode of Citrate in the Stabilization of Gold Nanoparticles. *Nat. Chem.* **2017**, *9*, 890.

(25) Pohjolainen, E.; Chen, X.; Malola, S.; Groenhof, G.; Hkkinen, H. A Unified AMBER-Compatible Molecular Mechanics Force Field for Thiolate-Protected Gold Nanoclusters. *J. Chem. Theory Comput.* **2016**, *12*, 1342–1350.

(26) Hospital, A.; Faustino, I.; Collepardo-Guevara, R.; González, C.; Gelpí, J. L.; Orozco, M. NAFlex: A Web Server for the Study of Nucleic Acid Flexibility. *Nucleic Acids Res.* **2013**, *41*, W47–W55.

(27) Ivani, I. et al. Parmbsc1: A Refined Force Field for DNA Simulations. *Nat. Meth.* **2016**, *13*, 55–58.

(28) Galindo-Murillo, R.; Robertson, J. C.; Zgarbova, M.; Sponer, J.; Otyepka, M.; Jurecka, P.; Cheatham, r., T. E. Assessing the Current State of Amber Force Field Modifications for DNA. *J. Chem. Theory Comput.* **2016**, *12*, 4114–27.

(29) Wang, J.; Wang, W.; Kollman, P. A.; Case, D. A. Automatic Atom Type and Bond Type Perception in Molecular Mechanical Calculations. *J. Mol. Graph. Model.* **2006**, *25*, 247 – 260.

(30) Darr, L.; Machado, M. R.; Dans, P. D.; Herrera, F. E.; Pantano, S. Another Coarse Grain Model for Aqueous Solvation: WAT FOUR? *J. Chem. Theory Comput.* **2010**, *6*, 3793–3807.

(31) Darr, L.; Tek, A.; Baaden, M.; Pantano, S. Mixing Atomistic and Coarse Grain Solvation Models for MD Simulations: Let WT4 Handle the Bulk. *J. Chem. Theory Comput.* **2012**, *8*, 3880–94.

(32) Head-Gordon, T.; Hura, G. Water Structure from Scattering Experiments and Simulation. *Chem. Rev.* **2002**, *102*, 2651–2670.

(33) Abraham, M. J.; Murtola, T.; Schulz, R.; Pll, S.; Smith, J. C.; Hess, B.; Lindahl, E. GROMACS: High Performance Molecular Simulations through Multi-level Parallelism from Laptops to Supercomputers. *SoftwareX* **2015**, *12*, 19 – 25.

(34) Humphrey, W.; Dalke, A.; Schulten, K. VMD – Visual Molecular Dynamics. *J. Mol. Graphics* **1996**, *14*, 33–38.

(35) Cruz-Aguado, J. A.; Penner, G. Determination of Ochratoxin A with a DNA Aptamer. *J. Agric. Food Chem.* **2008**, *56*, 10456–10461.

(36) Schalley, C. A. *Analytical Methods in Supramolecular Chemistry*; Wiley-VCH: Weinheim, 2012.

(37) Rhinehardt, K. L.; Srinivas, G.; Mohan, R. V. Molecular Dynamics Simulation Analysis of Anti-MUC1 Aptamer and Mucin 1 Peptide Binding. *J. Phys. Chem. B* **2015**, *119*, 6571–6583.

(38) Li, W.; Nordenskiold, L.; Mu, Y. Sequence-Specific Mg^{2+}−DNA Interactions: A Molecular Dynamics Simulation Study. *J. Phys. Chem. B* **2011**, *115*, 14713–14720.

(39) Wright, L. B.; Rodger, P. M.; Walsh, T. R. Structure and Properties of Citrate Overlayers Adsorbed at the Aqueous Au(111) Interface. *Langmuir* **2014**, *30*, 15171–15180.

(40) Brust, M.; Walker, M.; Bethell, D.; Schiffrin, D. J.; Whyman, R. Synthesis of Thiol-derivatised Gold Nanoparticles in a Two-phase Liquid-Liquid System. *J. Chem. Soc., Chem. Commun.* **1994**, 801–802.

(41) Storhoff, J. J.; Elghanian, R.; Mirkin, C. A.; Letsinger, R. L. Sequence-Dependent Stability of DNA-Modified Gold Nanoparticles. *Langmuir* **2002**, *18*, 6666–6670.

(42) Gourishankar, A.; Shukla, S.; Ganesh, K. N.; Sastry, M. Isothermal Titration Calorimetry Studies on the Binding of DNA Bases and PNA Base Monomers to Gold Nanoparticles. *J. Am. Chem. Soc.* **2004**, *126*, 13186–13187.

(43) Bogdan, D.; Morari, C. Electronic Properties of DNA Nucleosides Adsorbed on a Au(100) Surface. *J. Phys. Chem. C* **2012**, *116*, 7351–7359.

(44) Giese, B.; McNaughton, D. Surface-Enhanced Raman Spectroscopic and Density Functional Theory Study of Adenine Adsorption to Silver Surfaces. *J. Phys. Chem. B* **2002**, *106*, 101–112.

(45) Bogdan, D.; Morari, C. Effect of van der Waals Interaction on the Geometric and Electronic Properties of DNA Nucleosides Adsorbed on Cu(111) Surface: A DFT Study. *J. Phys. Chem. A* **2013**, *117*, 4669–4678.

(46) Zhang, X.; Servos, M. R.; Liu, J. Surface Science of DNA Adsorption onto Citrate-Capped Gold Nanoparticles. *Langmuir* **2012**, *28*, 3896–3902.

(47) Pergolese, B.; Bonifacio, A.; Bigotto, A. SERS Studies of the Adsorption of Guanine Derivatives on Gold Colloidal Nanoparticles. *Phys. Chem. Chem. Phys.* **2005**, *7*, 3610–3613.

(48) Zhang, X.; Sun, C. Q.; Hirao, H. Guanine Binding to Gold Nanoparticles through Nonbonding Interactions. *Phys. Chem. Chem. Phys.* **2013**, *15*, 19284–19292.

(49) Cha, H.; Yoon, J. H.; Yoon, S. Probing Quantum Plasmon Coupling using Gold Nanoparticle Dimers with Tunable Interparticle Distances Down to the Subnanometer Range. *ACS Nano* **2014**, *8*, 8554–8563.

(50) Zuloaga, J.; Prodan, E.; Nordlander, P. Quantum Description of the Plasmon Resonances of a Nanoparticle Dimer. *Nano Lett.* **2009**, *9*, 887–891.

(51) Esteban, R.; Borisov, A. G.; Nordlander, P.; Aizpurua, J. Bridging Quantum and Classical Plasmonics with a Quantum-corrected Model. *Nat. Commun.* **2012**, *3*, 825.

(52) Zhu, W.; Esteban, R.; Borisov, A. G.; Baumberg, J. J.; Nordlander, P.; Lezec, H. J.; Aizpurua, J.; Crozier, K. B. Quantum Mechanical Effects in Plasmonic Structures with Subnanometre Gaps. *Nat. Commun.* **2016**, *7*, 11495.

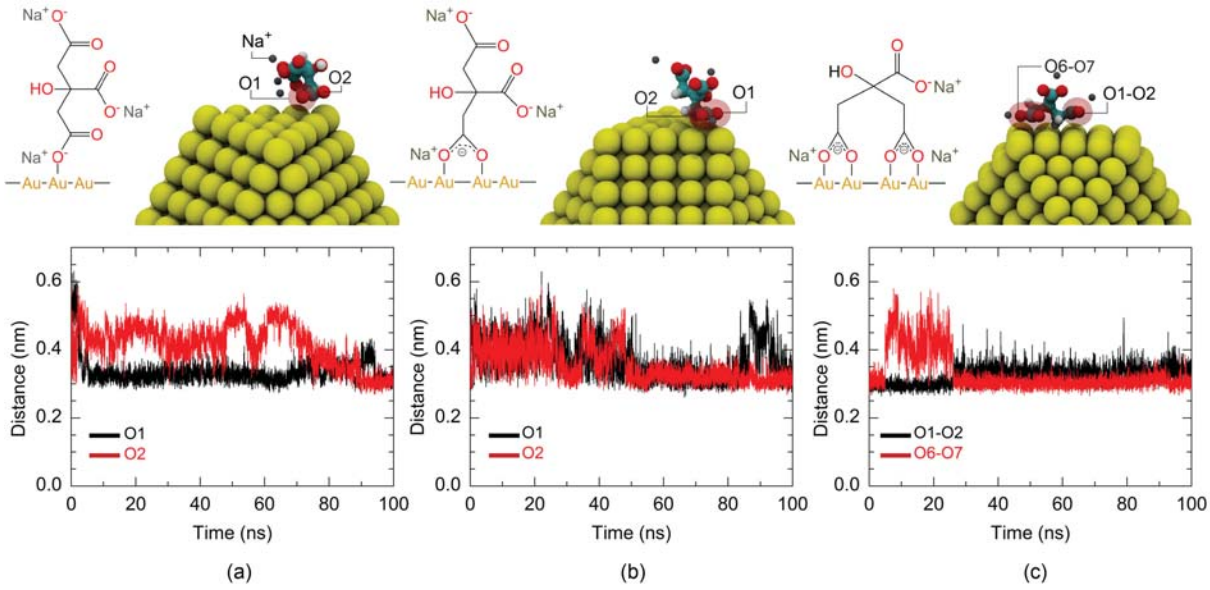

Figure 4: Binding of citrate on AuNP surface and assignment of the various citrate binding modes. The calculation of the distance between oxygen atoms (red) and Au(111) surface are performed in 100 ns. (a) monocarboxylate monodentate $1\kappa O^1$ (κ), (b) monocarboxylate bridging $\mu_2 - 1\kappa O^1 : 2\kappa O^3(\mu_2)$ and (c) dicarboxylate bridging $\mu_4 - 1\kappa O^1 : 2\kappa O^3 : 3\kappa O^{1'} : 4\kappa O^{3'}(\mu_4)$.

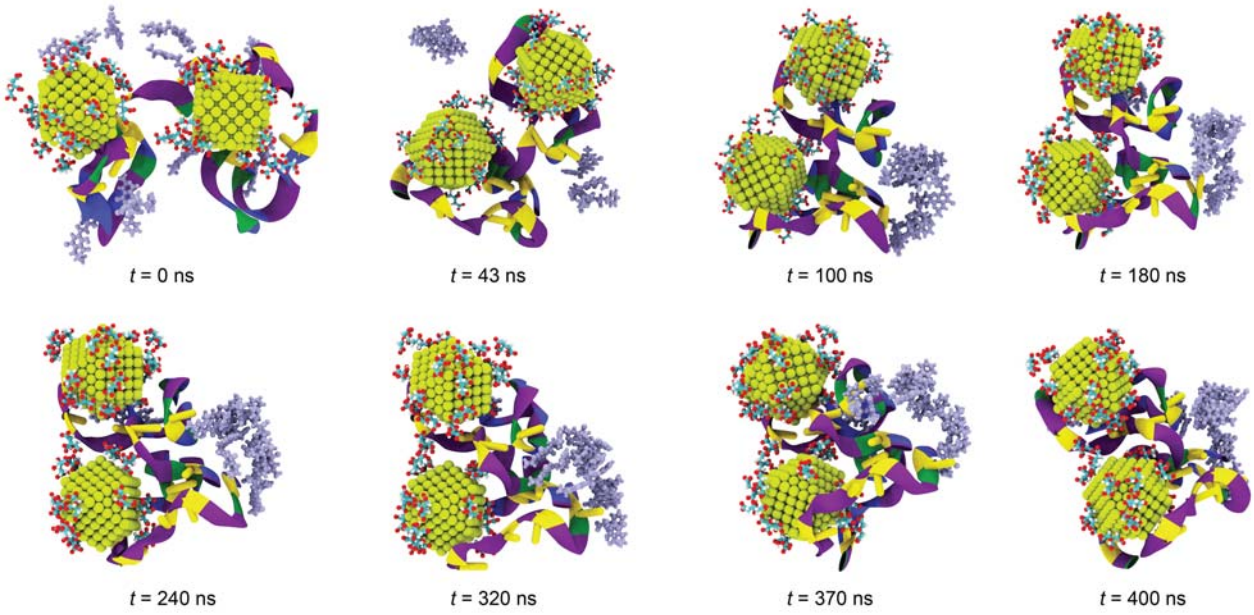

Figure 8: Snapshots of assembly of citrated-capped AuNPs (D = 2 nm) obtained from a 400 ns MD simulation (without water or ions). Thirty OTA molecules were placed into the simulation box but only eleven molecules (light purple) are shown for clarity. OTA molecules induce the formation of a structure in the anti-OTA aptamer and form the OTA-aptamer complex structure. The aptamer cannot protect the AuNPs from salt-induced aggregation resulting in the assembly of AuNPs. The interparticle distance (d) is decreased with increasing simulation time. The color code of oligonucleotide represents different bases. Adenine (A), thymine (T), cytosine (C) and guanine (G) correspond to blue, yellow, green and purple, respectively.

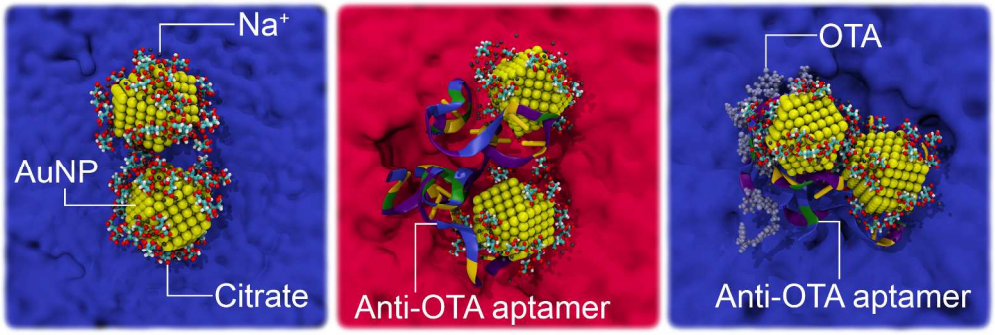

The sensing mechanism of AuNP-based colorimetric aptasensor for OTA detection.

262x88mm (300 x 300 DPI)